

















POWER SPECTRA OF JWST IMAGES OF LOCAL GALAXIES: SEARCHING FOR DISK THICKNESS

BRUCE G. ELMEGREEN ¹, ANGELA ADAMO ², VARUN BAJAJ ³, ANA DUARTE-CABRAL ⁴, DANIELA CALZETTI ⁵,
 MICHELE CIGNONI ^{6,7,8}, MATTEO CORRENTI ^{9,10}, JOHN S. GALLAGHER, III ¹¹, KATHRYN GRASHA ^{12,13}, BENJAMIN
 GREGG ⁵, KELSEY E. JOHNSON ¹⁴, SEAN T. LINDEN ¹⁵, MATTEO MESSA ⁶, GÖRAN ÖSTLIN ², ALEX PEDRINI ²,
 AND JENNA RYON ³

¹Katonah, NY 10536, USA

²Department of Astronomy, The Oskar Klein Centre, Stockholm University, AlbaNova, SE-10691 Stockholm, Sweden

³Space Telescope Science Institute, 3700 San Martin Drive Baltimore, MD 21218, USA

⁴School of Physics & Astronomy, Cardiff University, Queen’s Building, The Parade, Cardiff CF24 3AA, UK

⁵Department of Astronomy, University of Massachusetts Amherst, 710 North Pleasant Street, Amherst, MA 01003, USA

⁶INAF—Osservatorio di Astrofisica e Scienza dello Spazio di Bologna, Via Gobetti 93/3, I-40129 Bologna, Italy

⁷Department of Physics, University of Pisa, Largo B. Pontecorvo 3, 56127 Pisa, Italy

⁸INFN, Largo B. Pontecorvo 3, 56127 Pisa, Italy

⁹INAF Osservatorio Astronomico di Roma, Via Frascati 33, 00078 Monteporzio Catone, Rome, Italy

¹⁰ASI-Space Science Data Center, Via del Politecnico, I-00133 Rome, Italy

¹¹Department of Physics and Astronomy, Macalester University, 1600 Grand Avenue, Saint Paul, MN 55105-1899, USA

¹²Research School of Astronomy and Astrophysics, Australian National University, Canberra, ACT 2611, Australia

¹³ARC Centre of Excellence for All Sky Astrophysics in 3 Dimensions (ASTRO 3D), Australia

¹⁴Department of Astronomy, University of Virginia, Charlottesville, VA, USA and

¹⁵Steward Observatory, University of Arizona, 933 N Cherry Avenue, Tucson, AZ 85721, USA

Version November 12, 2024

ABSTRACT

JWST/MIRI images have been used to study the Fourier transform power spectra (PS) of two spiral galaxies, NGC 628 and NGC 5236, and two dwarfs, NGC 4449 and NGC 5068, at distances ranging from 4 to 10 Mpc. The PS slopes on scales larger than 200 pc range from -0.6 at $21\mu\text{m}$ to -1.2 at $5.6\mu\text{m}$, suggesting a scaling of region luminosity with size as a power law with index ranging from 2.6 to 3.2, respectively. This result is consistent with the size-luminosity relation of star-forming regions found elsewhere, but extending here to larger scales. There is no evidence for a kink or steepening of the PS at some transition from two-dimensional to three-dimensional turbulence on the scale of the disk thickness. This lack of a kink could be from large positional variations in the PS depending on two opposite effects: local bright sources that make the slope shallower and exponential galaxy profiles that make the slope steeper. The sources could also be confined to a layer of molecular clouds that is thinner than the HI or cool dust layers where PS kinks have been observed before. If the star formation layers observed in the near-infrared here are too thin, then the PS kink could be hidden in the broad tail of the JWST point spread function.

1. INTRODUCTION

The power spectrum (PS) of interstellar gas emission reveals the relative importance of structures and their luminosities over a wide range of scales, as measured by the Fourier transform wavenumber, k , which is the inverse of length. An important signature originally observed in the LMC (Elmegreen et al. 2001; Block et al. 2010), M33 (Combes et al. 2012), and the dwarf galaxy NGC 1058 (Dutta et al. 2009a) is the transition from two to three dimensions at wavenumbers exceeding the inverse disk thickness. Numerical simulations confirm this signature (Padoan et al. 2001; Bournaud et al. 2010; Combes et al. 2012), which is shown schematically in Figure 1. With such a signature in the power spectrum, the thicknesses of face-on galaxies can be inferred and mapped, as recently demonstrated for the LMC (Szkotkowski et al. 2019). Thickness can be important, for example, in converting gas surface density into volume density for determination of the local gas free-fall time (Bacchini et al. 2020), or for correcting an observed rotation curve for ra-

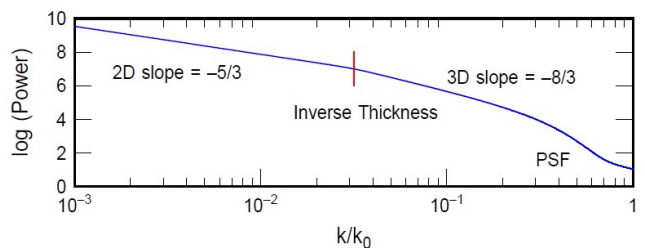


FIG. 1.— Schematic of the PS of a galaxy disk with a shallow slope at small wavenumber k , from 2D turbulence, representing large scales, and a larger slope at large k from 3D turbulence. The dip at high k from the point spread function is also shown. Equations 2 and 3 in Koch et al. (2020) were used.

dial pressure gradients in order to assess the distribution and amount of dark matter (Verbeke et al. 2017).

The explanation for the change in PS slope at the size scale of the disk thickness was illustrated in Bournaud et al. (2010) and Fensch et al. (2023) as the result of three components of turbulent velocity producing structure on small scales and two components of velocity producing

structure on large scales. Turbulent energy is also dispersed into a larger volume of phase space in 3D than in 2D, making the energy cascade steeper in 3D.

To see the disk thickness in a PS, the spatial resolution of the galaxy has to exceed the disk thickness by an order of magnitude or more. Then the slope of the steeper PS at high k can be distinguished from the slope of the shallower PS at low k . The ratio of the galaxy size to the thickness should also exceed a factor of ~ 10 , so there is another order of magnitude at small k , i.e., on lengths larger than the thickness. These two constraints are somewhat incompatible for a given angular resolution, because galaxies close enough to resolve for the first constraint tend to be dwarfs, which are also typically too thick (van den Bergh 1988) to satisfy the second constraint.

A third requirement to see disk thickness in a PS is that the emission should come from sources that are related to correlated motions such as interstellar turbulence, and not thermal motions as in warm or hot gas. Random stellar motions should not show the disk thickness in a PS. Thus the PS of light from old stars would not have a kink at the disk thickness, but the PS of star-forming regions traced by young stars could have it because of the turbulent structure of the gas that forms these stars. Thickness signatures in the PS of spiral galaxies observed at high resolution in the B-band are an example (Elmegreen et al. 2003a,b). On the other hand, there were no significant kinks in the PS of 9 dwarfs studied at V band by Willett et al. (2005), presumably because these galaxies are relatively thick on the line of sight. The $H\alpha$ images in Willett et al. (2005) had power-law PS with slopes that decreased from near-zero (characteristic of noise) to the same negative values as the V-band images, which was -1.4 ± 0.3 for one-dimensional scans, as the $H\alpha$ filling factor increased from ~ 0 to ~ 1 with the star formation rate.

Here we investigate the PS of JWST images of dust emission from nearby galaxies at $5.6\mu\text{m}$ to $21\mu\text{m}$ wavelength. We use data on NGC 628, NGC 4449, and NGC 5236 from the ‘‘Feedback in Emerging extrAgalactic Star clusTers’’ (FEAST) survey, and additional data for NGC 628 and a nearby galaxy, NGC 5068, from the PHANGS-JWST survey (GO 2107, Lee et al. 2023). These galaxies have the potential to satisfy all three of the above requirements to measure the disk thickness because of the high angular resolution of JWST and the small distances. However, problems can arise if the broad wings of the Point Spread Function (PSF) blend with the thickness scale, or if the closest galaxies are intrinsically thick.

Two of our galaxies were studied before. Dutta et al. (2008) measured the 2D PS of HI emission from NGC 628, finding a continuous slope of -1.6 ± 0.2 from 8 kpc to 800 pc – too large to observe a possible thickness effect at ~ 200 pc. Also, Nandakumar & Dutta (2020) measured the HI column density PS and velocity PS in NGC 5236, obtaining a continuous slope of -1.23 ± 0.06 for the column density structure from 11 kpc to 300 pc.

The PS has also been determined for several other galaxies at various wavelengths. In the first galaxy-scale measurement, Stanimirović et al. (1999) observed HI emission from the Small Magellanic Cloud (SMC) and found a continuous 2D PS with a slope of -3.04 ± 0.02 in narrow velocity intervals over spatial scales from 30 pc

to 4 kpc (see also Pingel et al. 2022). The slope steepens with increasing velocity width, allowing a separation of the PS for velocity and density (Lazarian & Pogosyan 2000; Dutta 2015). The density alone had a PS slope of -3.3 ± 0.01 from the integrated velocity map (Stanimirović & Lazarian 2001), which is about the same as that obtained from a dust column density map of the SMC (Stanimirović et al. 2000). In the Magellanic bridge, Muller et al. (2004) measured a power-law PS in the southwest region over scales from 29 pc to 2 kpc, finding a slope equal to -3.02 ± 0.14 for narrow velocity channels and steepening to -3.4 for the full velocity width. The northern region of the Magellanic bridge has a shallower slope.

In the dwarf DDO 210, Begum et al. (2006) found a 2D HI PS slope of -2.75 ± 0.45 from 80 pc to 500 pc. They suggested that the similarity of this slope to the slopes in the LMC, SMC and Milky Way implies that interstellar structure is independent of the star formation rate. Dutta et al. (2009b) also reported the 2D HI PS for seven dwarfs and one spiral, obtaining slopes ranging from -1.5 in And IV, NGC 628, UGC 4459, and GR 8 to -2.6 in DDO 210 and NGC 3741. They interpreted the shallow slopes as the result of 2D turbulence in galaxies where the thickness could not be resolved and the steep slopes as the result of 3D turbulence everywhere for intrinsically thick galaxies. They noted that the shallow slope correlates with the star formation rate per unit area, with larger rates corresponding to steeper slopes. Such a correlation between star formation rate and slope was also noted for various regions around the LMC by Szołkowski et al. (2019), who suggested that star formation feedback destroys small scale structure in HI.

Zhang et al. (2012) determined 2D PS of HI for 24 dwarf irregular galaxies over single velocity channels and over the integrated velocities. The length scales typically ranged between several hundred pc and several kpc but in some cases were smaller. There were no kinks suggesting thickness for these galaxies, but the larger galaxies systematically had shallower slopes, as if they were everywhere thin on the line of sight compared to the smaller galaxies, which could be thicker. The division between these cases occurred at a star formation rate of $10^{-2.1} M_{\odot} \text{ yr}^{-1}$ and an absolute magnitude of $M_B = -14.5$ mag. The slopes also varied from a constant value at large velocity widths to shallower values at narrow velocity widths, which suggested relatively more small-scale structure beyond the limit of velocity resolution resulting from cool neutral gas, particularly in the inner galactic regions. Zhang et al. (2012) noted that although the slopes depended on absolute SFR as a result of galaxy size, they were independent of the average SFR surface density, which led them to suggest that non-stellar power sources drive the implied turbulence. A similar conclusion was reached by Nestingen-Palm et al. (2017) for the SMC.

Spiral galaxies have also had PS measurements in HI, but usually without the resolution necessary to see a feature from disk thickness. Dutta et al. (2010) calculated the HI PS for NGC 4254, finding a slope of -1.7 on scales ranging from 1.7 kpc to 8.4 kpc. They suggested NGC 4254 is a harassed galaxy, and noted that the PS slope in the outer parts, -2.0 ± 0.3 , is steeper than in the inner parts, -1.5 ± 0.2 . Dutta et al. (2013a) measured the HI

PS slopes for 18 spiral galaxies over scales ranging from several hundred pc to 16 kpc; the PS were power laws with slopes of around -1.3 , which they concluded was from 2D turbulence. Dutta et al. (2013b) then showed how to convert the amplitude of the PS to the HI mass fraction. More recently, Nandakumar & Dutta (2023) measured a PS slope of -0.96 ± 0.05 for HI column density and -1.81 ± 0.07 for velocity in NGC 6946. They suggested a driving scale larger than 6 kpc, with magnetic processes contributing to solenoidal motions and gravitational processes contributing to compressive motions.

The PS kink as a tracer of disk thickness has been questioned by Koch et al. (2020), who looked at FIR emission maps and dust surface densities maps of the LMC, SMC, M31 and M33. The most important test was for the LMC because the SMC has no kink in HI and the spatial resolutions for M31 and M33 were comparable to their expected thicknesses. For the LMC, Koch et al. (2020) suggest the PS is a continuous power law outside of the 30 Dor region, and the kink in the whole galaxy PS comes from 30 Dor. Szotkowski et al. (2019) map the PS slopes over the LMC and also get a steeper PS near 30 Dor, but they also find PS kinks elsewhere in the LMC.

In summary, the previous observations rarely detected a disk thickness from two components of the PS. Usually the PS had one continuous power law from scales of multiple kpc down to the resolution limit, which was typically larger than the expected thickness of several hundred pc. The continuous power law still gave important information, however, confirming expectations from 2D turbulence theory and pointing to very large driving scales at the lowest wavenumbers. This implied there are large-scale energy sources and continuous energy cascades or structural hierarchies below that.

2. FEAST SURVEY

The FEAST survey is a cycle-1 JWST program (GO 1783, PI Adamo) designed to map the early stages of star cluster formation in six representative local galaxies. JWST observations with NIRCcam and MIRI cameras sample the continuum, H recombination lines ($P\alpha$ and $Br\alpha$), and three bands from 1 to 8 μm (Adamo et al in prep.). In the present paper, we use the MIRI observations in F560W and F770W filters for NGC 628, NGC 4449, and NGC 5236, and MIRI data also in F1000W and F2100W for NGC 628 from PHANGS-JWST (Lee et al. 2023). Relevant parameters for all the galaxies considered here are in Table 1.

The MIRI observations consist of mosaics of 1×5 or 1×3 tiles and are completed with external background observations. Stage-two pipeline frames of the background were used to create a master background for each of the MIRI filters, and then subtracted from single target exposures during level-two processing. We conducted the sky matching step between different exposures using *PixelSkyMatchStep* (Bajaj 2023). The remainder of the level-three processing created a single mosaic for each filter. The final MIRI mosaics are resampled to a scale of $0.08''/\text{px}$.

We also include in this analysis archival MIRI observations of NGC 5068 from the PHANGS-JWST cycle 1 large program, available at $0.11''$ pixel size (Lee et al.

TABLE 1
GALAXY SAMPLE AND SCAN DETAILS

Galaxy NGC	Dist. Mpc	Filter	Pixel //	FWHM pc ^a	Length pixels	Number of scans
628	9.84	F560W	0.08	9.9	1408	4055
628	9.84	F770W	0.08	12.8	1408	4055
628	9.84	F1000W	0.08	15.6	1546	2734
628	9.84	F2100W	0.08	32.1	1546	2734
5236	4.66	F560W	0.08	4.7	1472	4232
5236	4.66	F770W	0.08	6.1	1472	4232
4449	4.27	F560W	0.08	4.3	1517	2530
4449	4.27	F560W	0.08	4.3	2444 ^b	1517 ^b
4449	4.27	F770W	0.08	5.6	1516	2530
4449	4.27	F770W	0.08	5.6	2444 ^b	1517 ^b
5068	5.2	F1000W	0.11	8.3	1380	1908
5068	5.2	F2100W	0.11	17.0	1380	1908

^aFWHM resolutions in pc, converted from the arcsec FWHM in the JWST User Documentation (see footnote 1), using the distances.

^b Major axis intensity scan.

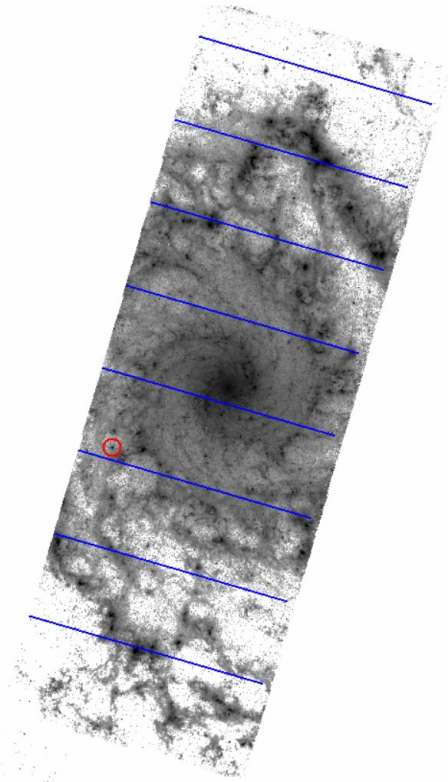


FIG. 2.— NGC 628 at $5.6\mu\text{m}$ with sample scan directions like those used to determine the PS. The separation between lines is 500 pixels, which is $40''$, or 1.91 kpc. The red circle shows the bright source used to show the PSF at $5.6\mu\text{m}$.

2023). The mosaics consisted of 1×3 tiles and 1 external background observation. Data acquisition and reduction are described in Williams et al. (2024) and data are accessible at the repository <https://archive.stsci.edu/hlsp/phangs/phangs-jwst>.

3. ONE-DIMENSIONAL POWER SPECTRA OF NGC 628 AT 5.6 MICRONS

3.1. Intensity Scans

Figure 2 shows a wide swath through the center of NGC 628 taken with the JWST F560W filter. The nominal Full Width at Half Maximum (FWHM) of the PSF is $0.207''$ from the JWST User Documentation¹. This FWHM corresponds to 2.59 pixels and 9.9 pc at the distance of 9.84 Mpc to NGC 628 (from Leroy et al. 2021; Tully et al. 2009). Overlaid on the image are 8 lines showing representative locations of intensity scans used to determine one-dimensional PS. Each scan is 1408 pixels long, and for the entire length of the swath, there are 4055 such scans (scan parameters for all of the galaxies are in Table 1). The figure shows every 500th scan. Also shown is a red circle surrounding a small bright source that will be used to illustrate the PSF.

We use 1D intensity scans for the PS in order to get a long length but not cover a large area, which might include several types of regions. We expect the dust disk scale height to be in a range from 100 pc to 300 pc based on NIR and CO images of the edge-on galaxy NGC 891 (Scoville et al. 1993; Bocchio et al. 2016; Elmegreen & Elmegreen 2020; Chasten et al. 2024). This scale corresponds to a range from 26 pixels to 79 pixels for NGC 628, so a scan 1408 pixels long will have a presumed break point somewhere close to the middle on a plot of the log of the wavenumber. That is, $\log 26$ and $\log 79$ are 0.45 and 0.60 times $\log 1408$, respectively. Thus the indicated scans are the right length to show a PS kink if there is one. Taking all ~ 4000 scans along the length of the swath effectively maps the PS and any thickness indicators over the face of the disk.

The intensity along a scan was sampled with 1 pixel spacing, but the scan pixels are not exactly the same as the image pixels. To determine the intensity at the center of a scan pixel, we averaged over the values in the scan pixel and the nearest 3 other pixels, using weights proportional to the pixel areas included within ± 0.5 pixel of the scan pixel. Each scan had the same length with endpoints that lied entirely within the image and no zeros at either end. The scans were perpendicular to the long axis of the image swath as determined by finding the transitions from zero values to non-zero values along the eastern edge. The line of these transitions defined the direction of the swath and the starting pixel of each scan. We note that the data have been cleaned in the reduction process so there are no bad pixels, which may be expected towards the edges of the detectors.

The blue curves in Figure 3 show intensity scans for the 8 equally-spaced positions corresponding to the lines in Figure 2. The red curve is the intensity scan through the bright source at $1^{\text{h}}36^{\text{m}}45.46^{\text{s}}$, $15^{\circ}46'33.43''$, which is shown by the red circle in Figure 2. The bright-source intensity has been divided by 20 to fit on the axes.

The left-hand panel of Figure 4 shows the scan through the bright source again, along with an image of this source as an insert. The right-hand panel has an enlargement of the source profile as a red curve and, as a black curve, the average scan through a 2D PSF that was independently fit to our observations (as a 45×45 pixel image) from known point sources outside the galaxy. The intensity profile of the bright source matches well the idealized

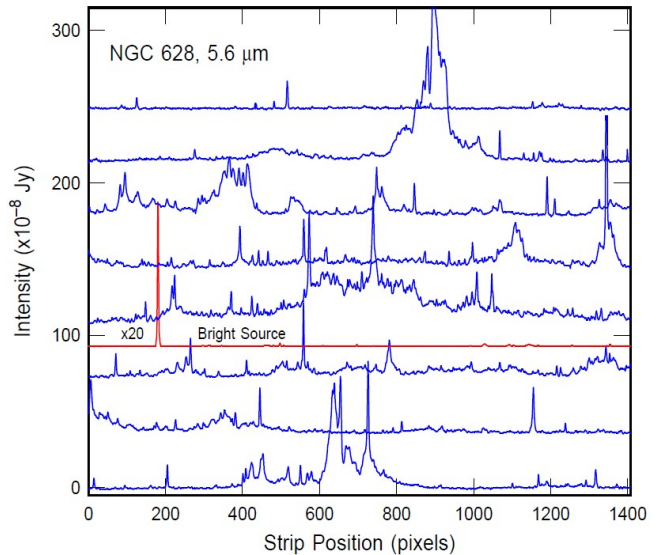


FIG. 3.— Intensity scans across the $5.6\mu\text{m}$ image of NGC 628, shifted vertically from bottom (south) to top (north) for better viewing, that correspond to the blue lines in Fig. 2. The red curve, plotted at 1/20th scale compared to the others, corresponds to the intensity scan through the bright $5.6\mu\text{m}$ source indicated by the red circle in the previous image.

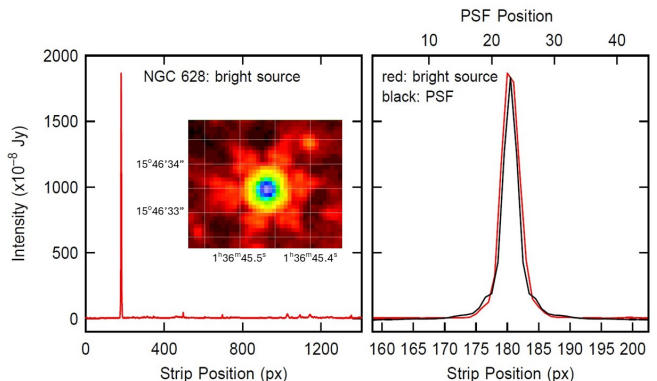


FIG. 4.— (Left:) The red curve is the same intensity scan as that shown by a red curve in Fig. 3. It is one pixel wide and goes through the small bright source indicated by the red circle in Fig. 2. The insert shows the source itself; the coordinates are $1^{\text{h}}36^{\text{m}}45.46^{\text{s}}$, $15^{\circ}46'33.43''$. (Right:) The red curve is a blow-up of the same scan highlighting the bright source, and the black curve is a scan through an idealized PSF made from bright point sources in the same image. The strip position on the lower abscissa is in reference to the bright-source scan through the galaxy, while the PSF position at the top is in reference to the idealized two-dimensional PSF, which is 45 pixels wide. The bright source is small, nearly point-like, and much brighter than the other galaxy sources in the same scan, so it is a good match to the PSF.

PSF.

3.2. Power Spectra

Power spectra were determined for each intensity scan by summing over the products of the intensity with sine and cosine functions. We experimented with a correction for the different intensities at the beginnings and ends of each scan, which are viewed by a Fourier transform as a sudden jump between neighboring pixels. In this experiment, we attached cosine functions to each end with values of zero at the far ends and values equal to the scan values where they attached. The wavelength of this

¹ <https://jwst-docs.stsci.edu/jwst-mid-infrared-instrument/miri-performance/miri-point-spread-functions>

cosine function was twice the scan length, making a half-wave modifier at each end and a new scan with twice the length of the original scan. With this replacement, the intensity jump between the beginning and ending pixels contributes only to the Fourier transform at the lowest k value. However, applications of this cosine-padding method to the scan with the bright source introduced too large a signal at small k , giving the PS of the PSF a slightly negative slope instead of zero slope without the cosine padding. Also, many of the scans have intensities close to sky values at the ends, so the end-to-end jumps viewed by the Fourier transform were no more severe than any other pixel-to-pixel jumps from noise. For these reasons we do not include cosine padding for the results presented here. The primary change to the intensity scans was to subtract the average value, giving zero average for each before the Fourier transform. The relative scan amplitudes were not changed, so the averages of PS presented below are weighted by the brighter scans.

The sine and cosine functions are evaluated by direct summations:

$$S(k) = \frac{1}{N} \sum_{m=1}^N I(m) \sin(2\pi km/N) \quad (1)$$

$$C(k) = \frac{1}{N} \sum_{m=1}^N I(m) \cos(2\pi km/N)$$

for wavenumber $k = 1, N/2$. The largest k value corresponds to a wavelength consisting of 2 pixels, representing the two halves of the shortest complete sine wave. In what follows, we call this largest k value k_0 and normalize the other k values to it, plotting k/k_0 . The power spectrum is

$$P(k) = S(k)^2 + C(k)^2. \quad (2)$$

Figure 5 shows in blue color the 8 PS that correspond to the 8 intensity scans in Figure 3. Each PS is noisy so we average together the 50 PS surrounding these scans (from ± 25 strips) to make a single PS with higher signal-to-noise. These are shown as red curves in Figure 5. At the top of the figure are the PS of the scan with the bright source (red curve) and the PS of the idealized PSF (black curve). There is PSF structure out to several arcsec that causes a dip in the PS at high k . The lower x-axis is the relative wavenumber, k/k_0 , and the upper x-axis shows the corresponding length scale in parsecs. A typical disk thickness of $\sim 100 - 300$ pc would be in the center of the scan on this logarithmic scale.

There is significant variation in the PS from scan to scan, reflecting the presence or lack of bright sources, including the disk itself for scans that go close to the galaxy center. Figure 6 shows all of the 50-PS averages, from the southeast part of the galaxy in the lower left of the figure, to the northwest part in the upper right. The average PS are spaced vertically by a constant amount for clarity; every tenth one is blue. They all have a dip at high k/k_0 from the PSF at $5.6\mu\text{m}$, but they vary in slope at low k/k_0 . The bright source is in scan 1550, which is in the 31st average PS. This is the 4th curve up from the bottom in the central panel. Other PS averages with bright sources have the same shape as this one, namely a near-zero slope at low k/k_0 and a greater-than-average drop at high k/k_0 from the PSF. There is no evidence for a kink in any of the average PS at a wavelength corre-

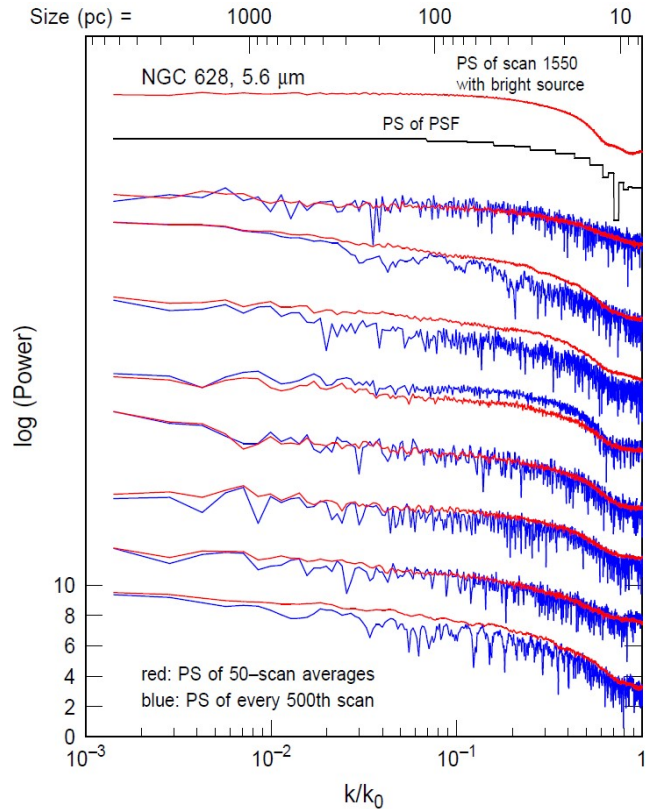


FIG. 5.— Blue: PS of the scans in Fig. 3, shifted vertically for better viewing. Red: Average of 50 PS centered on the PS of the Fig. 3 scans. The Fourier transform wavenumber is denoted by k , and the wavenumber corresponding to a wavelength of 2 pixels is denoted by k_0 . The dip at high k/k_0 is the PSF from small bright sources in the image. The black PS at the top is the PS of the idealized PSF, which is 45 pixels wide and stretched to fit this scale for NGC 628. The red PS at the top is the PS of the single intensity scan through the small bright source indicated by a red circle in Fig. 2.

sponding to the suspected disk thickness of $\sim 100 - 300$ pc.

The bottom panel of Figure 7 shows the slopes of the PS averages on scales larger than 200 pc. The average slope is -0.83 and the average error in the slope is 0.17, much smaller than the scatter. The dispersion in the slope is ± 0.31 . These values are in Table 2. The top panel shows the average intensities of all the scans, in blue, and the rms values around those averages, in red. The rms spikes when there is a bright source in the scan. The scan containing the brightest point-like source, scan 1550, is indicated by a vertical dashed line in the top panel and a red circle in the bottom panel. As was evident from previous figures, the slope of the PS of the bright source is ~ 0 on large scales. Other spikes in the rms correspond to shallow slopes too. Figure 7 also shows a systematically steeper (negative) slope for scans that go through the inner part of the galaxy. These scans include the exponential disk profile which is a large-scale structure, and that adds power at low k/k_0 , making the slope more negative. These more negative slopes are directly evident in Figure 6 around the 40th PS-average, which is in the middle of the central panel.

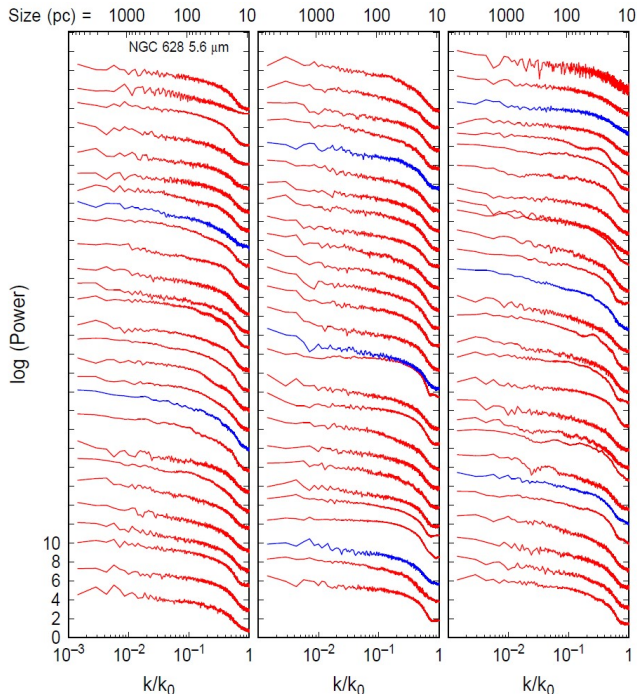


FIG. 6.— Averages of each 50 adjacent PS covering the image in Fig. 2, shifted vertically for clarity. The 50-PS average corresponding to the southeast part of the image is at the bottom of the left-hand panel. Higher in the same panel, and then from bottom to top in the middle panel and bottom to top in the right-hand panel are the 50-PS averages in sequence from southeast to northwest in the image. The blue curves denote every 10th 50-PS average, which correspond to the positions of the blue lines in Figure 2.

TABLE 2
POWER SPECTRUM RESULTS

Galaxy	Filter	Scan	50-PS Slope	50-PS
NGC		Direction	> 200 pc	Slope rms
628	F560W	Minor Axis	-0.83 ± 0.31	0.17
628	F770W	Minor Axis	-0.86 ± 0.26	0.20
628	F1000W	Minor Axis	-0.80 ± 0.25	0.19
628	F2100W	Minor Axis	-0.63 ± 0.34	0.15
5236	F560W	Minor Axis	-1.17 ± 0.59	0.39
5236	F770W	Minor Axis	-1.11 ± 0.51	0.41
4449	F560W	Minor Axis	-0.95 ± 0.43	0.29
4449	F560W	Major Axis	-0.91 ± 0.35	0.23
4449	F770W	Minor Axis	-0.99 ± 0.37	0.37
4449	F770W	Major Axis	-0.92 ± 0.33	0.26
5068	F1000W	Minor Axis	-0.80 ± 0.36	0.20
5068	F2100W	Minor Axis	-0.58 ± 0.37	0.15

4. POWER SPECTRA OF NGC 628 AT 7.7 MICRONS, 10 MICRONS AND 21 MICRONS

Now we consider the $7.7\mu\text{m}$, $10\mu\text{m}$, and $21\mu\text{m}$ images of NGC 628 taken with the F770W, F1000W, and F2100W filters as part of the FEAST and PHANGS-JWST programs. The pixel scales are still $0.08''$, but the nominal FWHM of the PSF is larger for longer wavelengths. For $7.7\mu\text{m}$, it is $0.269''$ or 3.36 pixels (12.8 pc), for $10\mu\text{m}$ it is $0.328''$ or 4.1 pixels (15.6 pc), and for $21\mu\text{m}$, it is $0.674''$ or 8.425 pixels (32.1 pc, see Table 1).

Images for $7.7\mu\text{m}$ and $10\mu\text{m}$ with sample scan lines are in Figures 1 and 3 in the Appendix, and 50-PS averages at these wavelengths are in the Appendix Figures 2 and 4. The slopes on scales larger than 200 pc (Table 2), and

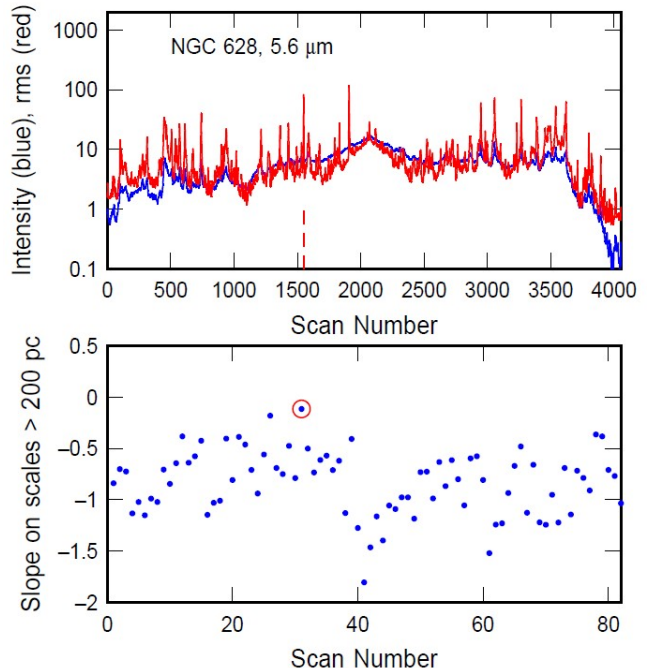


FIG. 7.— Bottom: Slopes of the low- k parts of the 50-PS averages for scales larger than 200 pc, versus the scan number from 1 to 82 corresponding to scans from southeast to northwest in the galaxy image of Fig. 2. Top: average intensity (blue) and rms (red) of each scan, in order from southeast to northwest. The dashed red line indicates the position of the bright source shown by a red circle in Fig. 2. Corresponding to this is the point in the bottom panel with the red circle. The PS slope at low- k is close to zero for the scan with the dominant point-like source. The PS slope systematically gets more negative for scans going through the galaxy center because of the disk exponential profile along the scan direction, which introduces significant power on large scales.

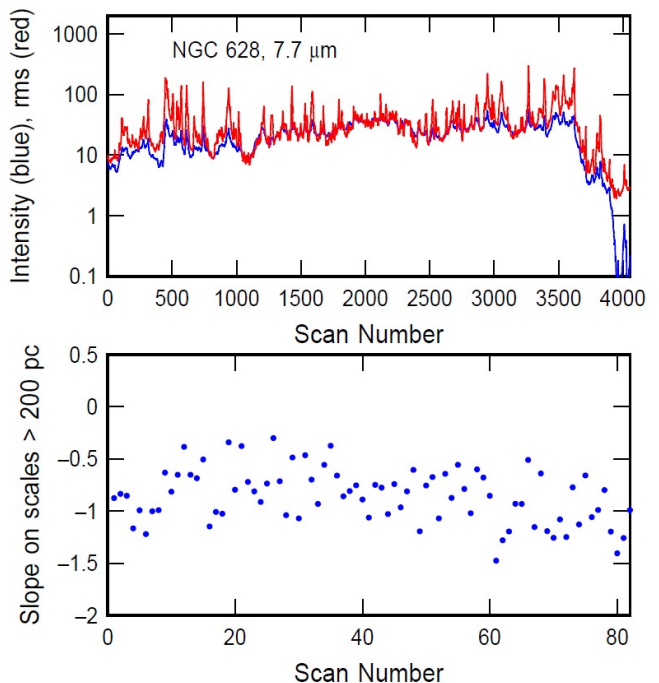


FIG. 8.— Same as figure 7 but for the $7.7\mu\text{m}$ image of NGC 628.

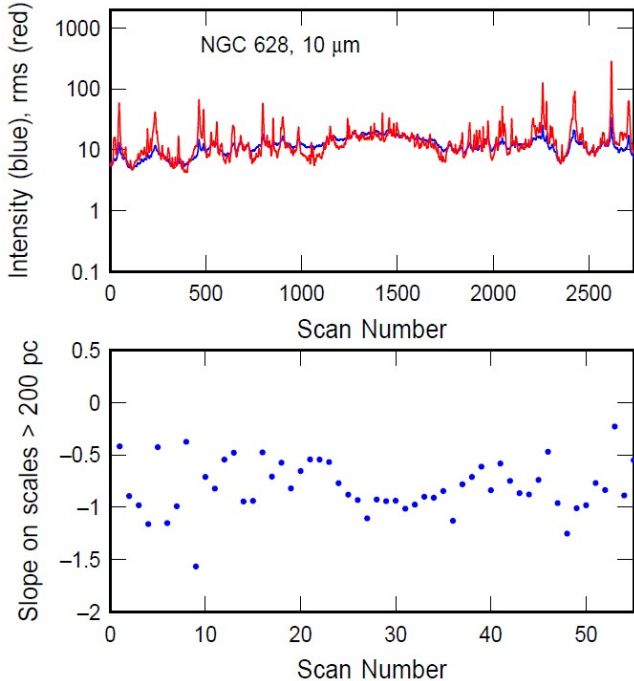


FIG. 9.— Same as figure 7 but for the $10\mu\text{m}$ image of NGC 628.

the mean intensities and rms values are in Figures 8 and 9, respectively. The intensity spikes are not as high at $7.7\mu\text{m}$ as at $5.6\mu\text{m}$, and the large-scale PS slopes are not as close to zero for the highest intensity spikes. Neither is there a significant influence by the exponential disk in steepening the slope in the central region of the galaxy. On the other hand, there are a few strong spikes in the $10\mu\text{m}$ image and one slope value close to zero at average-PS number 53 (lower panel on the right). There is also more evidence for the exponential disk in the $10\mu\text{m}$ PS going near the galaxy center.

The $21\mu\text{m}$ intensity is more spiked with bright sources than any of the others. Figure 10 shows the scan directions on the $21\mu\text{m}$ image. The image looks significantly different than the $5.6\mu\text{m}$ image in Figure 2 because of the relatively brighter spiral arms, spurs and star-forming regions at $21\mu\text{m}$. These differences are also reflected in the 50-PS average slopes in Figure 11, which are generally closer to zero than at shorter wavelengths, and in the relatively high rms values compared to the average intensities in the top panel. All of the 50-PS averages are in Appendix figure 5. Corresponding to the intensity spikes, there are many flat PS with steep drops into the PSF depression.

Comparing all of the 50-PS averages for NGC 628, there is a general trend toward flatter slopes on large scales for longer observed wavelengths, with slope averages (Table 2) varying as -0.83 ± 0.31 , -0.86 ± 0.26 , -0.80 ± 0.25 , and -0.63 ± 0.34 for $5.6\mu\text{m}$, $7.7\mu\text{m}$, $10\mu\text{m}$ and $21\mu\text{m}$, respectively. There is also an obvious extension of the PSF toward larger scales with longer wavelengths, even reaching the likely disk thickness close to ~ 100 pc at $21\mu\text{m}$. Nevertheless, there is no indication of a systematic thickness kink in these PS averages: most of the structure seems to come from discrete sources. There are a few 50-PS averages that have slight PS kinks at ~ 200 pc, but mostly the PS is curved in this range,

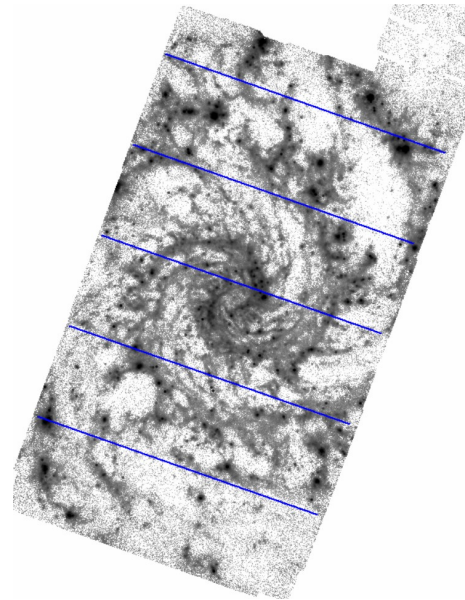


FIG. 10.— NGC 628 at $21\mu\text{m}$ with sample scan directions like those used to determine the PS. The separation between lines is 500 pixels, which is $40''$, or 1.91 kpc.

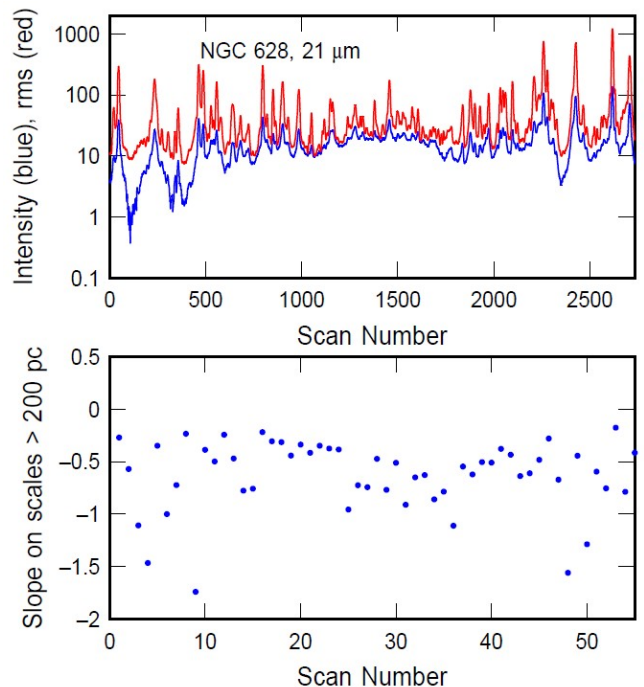


FIG. 11.— Same as figure 7 but for the $21\mu\text{m}$ image of NGC 628.

rather than kinked. We comment on a possible origin for the -0.6 to -0.9 slopes at large scales in Section 6.

5. POWER SPECTRA OF NGC 5236, NGC 4449, AND NGC 5068

A closer galaxy will have better spatial resolution than NGC 628. In the FEAST program, there is also the barred galaxy NGC 5236 at 4.66 Mpc (Tully et al. 2013) and the dwarf galaxy NGC 4449 at 4.27 Mpc (Tully et al. 2013) in $5.6\mu\text{m}$ and $7.7\mu\text{m}$ passbands. PHANGS-JWST (Lee et al. 2023) has another relatively close dwarf

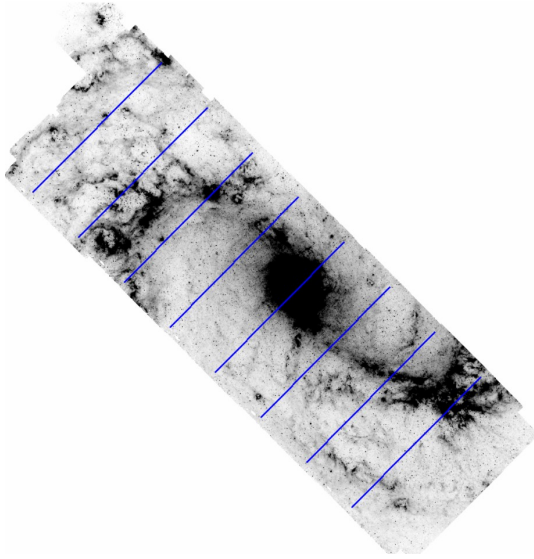


FIG. 12.— NGC 5236 at $5.6\mu\text{m}$ with sample scan directions like those used to determine the PS. The separation between lines is 500 pixels, which is $40''$, or 0.90 kpc.

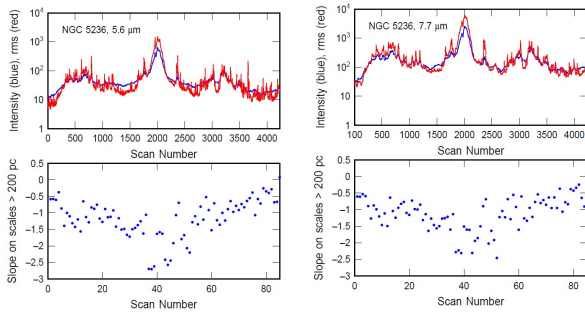


FIG. 13.— Low- k slopes of the 50-PS averages (bottom) and average scan intensities (blue) and rms values (red, top) for NGC 5236 at $5.6\mu\text{m}$ (left) and $7.7\mu\text{m}$ (right). The slopes become more negative for scans through the inner regions of the galaxy because they contain the exponential disk profile which has power on large scales.

galaxy, NGC 5068 at 5.2 Mpc, that has data at $10\mu\text{m}$ and $21\mu\text{m}$.

Scan directions through the $5.6\mu\text{m}$ image of NGC 5236 are shown in Figure 12, with scan numbers 500, 1000, 1500, etc., drawn as blue lines. The average intensities, rms values, and 50-PS average slopes are in Figure 13 for $5.6\mu\text{m}$ and $7.7\mu\text{m}$. This galaxy has a bright central region at both wavelengths where the PS slopes become steeper as a result of the exponential disk. Figures 6 and 7 in the Appendix show the 50-PS averages. There are few bright star forming regions that produce flat PS, and there is no systematic evidence for a kink in the PS indicative of disk thickness.

Figure 14 shows NGC 4449 at $5.6\mu\text{m}$ with minor and major axis scan directions to make PS with two different scan lengths (the blue lines are scan numbers 500, 1000, 1500, etc.). Figures 15 and 16 show average intensities, rms values, and large-scale slopes for these two scan directions, respectively. A bright source indicated by the red circle in Figure 14 corresponds to the intensity peaks and slopes indicated by dashed lines and red circles in Figures 15 and 16. Again, the large scale slope of the

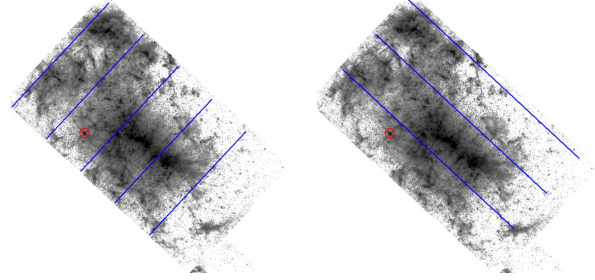


FIG. 14.— NGC 4449 at $5.6\mu\text{m}$ with sample scan directions like those used to determine the PS. Sample minor axis scans are on the left and major axis scans are on the right. In both cases, the lines are separated by 500 pixels, which is $40''$ or 0.83 kpc. The red circle denotes a bright source.

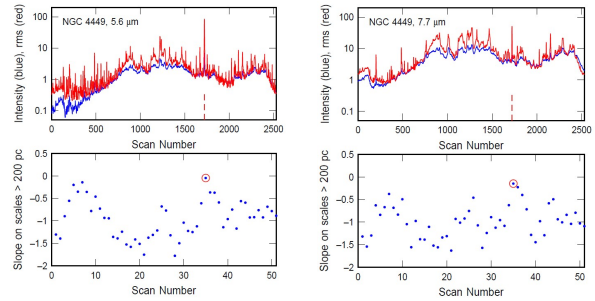


FIG. 15.— Low- k slopes of the 50-PS averages (bottom) and average scan intensities (blue) and rms values (red, top) for minor axis scans through NGC 4449 at $5.6\mu\text{m}$ (left) and $7.7\mu\text{m}$ (right).

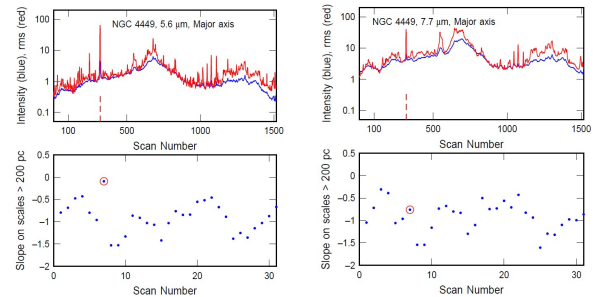


FIG. 16.— Low- k slopes of the 50-PS averages (bottom) and average scan intensities (blue) and rms values (red, top) for major axis scans through NGC 4449 at $5.6\mu\text{m}$ (left) and $7.7\mu\text{m}$ (right).

PS is close to 0 for the scan with the bright point-like source, and the PS get steeper through the central regions, which correspond to the range between scans 500 and 1000 for both scan directions.

Appendix Figures 8 to 11 show the 50-PS averages in all 4 cases for NGC 4449. The bright source has the flat and smooth PS at the lower part of the right hand panel for the minor axis PS (Figs. 8, 9), and the 7th PS up from the bottom of the left-hand panel for the major axis PS (Figs. 10, 11). There is no systematic indication of a kink in the 50-PS averages at what might be the disk thickness.

For NGC 5068, the pixel scale is $0.11''$. Figure 17 shows the scan directions for NGC 5068 on the $10\mu\text{m}$ image and Figure 18 shows the scan average intensities, rms values and large-scale slopes of the 50-PS averages. There are no particularly bright sources and no scans that clearly sample an exponential disk profile. All of the 50-PS averages are in Appendix Figures 12 and 13. Some of these averages have the flat-slope signature of a scan with a

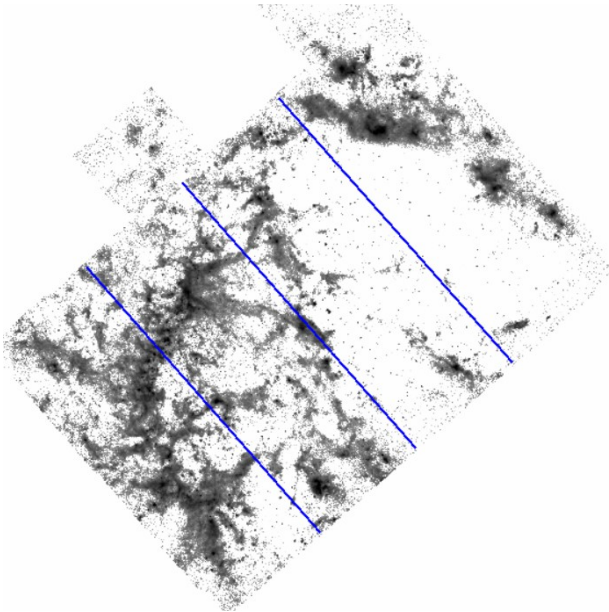


FIG. 17.— NGC 5068 at $10\mu\text{m}$ with sample scan directions like those used to determine the PS. The separation between lines is 500 pixels, which is $40''$, or 1.00 kpc.

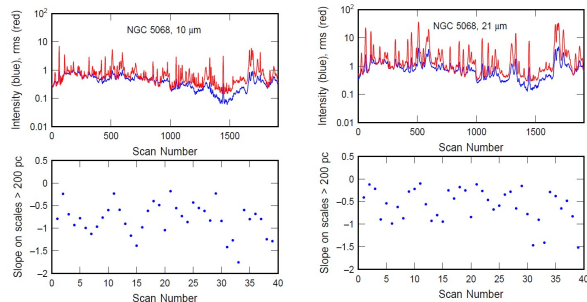


FIG. 18.— Low- k slopes of the 50-PS averages (bottom) and average scan intensities (blue) and rms values (red, top) for NGC 5068 at $10\mu\text{m}$ (left) and $21\mu\text{m}$ (right).

primary point-like source, even though excessively bright intensities do not show up in Figure 18. As for the other galaxies studied here, there are no obvious systematic kinks in the PS that might indicate the disk thickness.

6. DISCUSSION

6.1. Searching for a Thickness Kink in the PS

The PS of face-on galaxies have the potential to show the line-of-sight thickness, where two-dimensional turbulence converts to three-dimensional turbulence, but there are severe constraints on the suitability of this method. The PS needs a reasonably large factor for the range of wavenumbers on either side of the thickness kink, which implies a spatial resolution at least a factor of ~ 10 smaller than the galaxy thickness and a galaxy size at least a factor of ~ 10 larger than the thickness. An additional constraint is that the observations must sample some type of emission that follows the correlated structure of turbulent gas. These constraints were satisfied for HI and FIR emission from the LMC and M33, but they are difficult for other galaxies with the existing archive of data on the neutral component of the ISM.

The present study uses JWST observations of dust

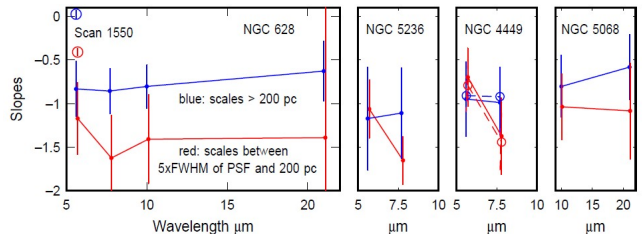


FIG. 19.— 50-PS average slopes for scales larger than 200 pc (blue) and for scales between 5 times the FWHM of the PSF (as listed in Table 1) and 200 pc (red) are shown versus the wavelength for all four galaxies. The rms range for each slope is shown by the error bars. Because 5 times the FWHM of the PSF at $21\mu\text{m}$ in NGC 628 (which corresponds to 160.5 pc) is close to 200 pc, there are very few k/k_0 values in this range and the rms is large, ± 2.1 , and mostly outside the figure. The two circles (with their tiny error bars) in the upper left corner are the slopes of the PS of scan 1550 for NGC 628 at $5.6\mu\text{m}$, which is the scan with the bright point-like source shown in Fig. 4. The red points are shifted to the right by $0.1\mu\text{m}$ for clarity.

emission at what is nominally sub-arcsec resolution from the full mirror diameter, which should be good enough to reach linear scales of several tens of parsecs for a large number of galaxies within 10 Mpc. However, the point spread function for the JWST image has a broad tail with a hexagonal shape from the mirror segments, and this PSF is ~ 5 times larger than the nominal FWHM. The PSF is visible as a strong dip in the PS at high wavenumbers, since there is no signal received by the detector on smaller scales, only noise. For the furthest of our galaxies, NGC 628 at 9.84 Mpc, this dip extends as a broad depression in the PS to ~ 50 pc ($5\times\text{FWHM}$) at $5.6\mu\text{m}$, and to ~ 64 pc, ~ 78 pc and ~ 160 pc at $7.7\mu\text{m}$, $10\mu\text{m}$, and $21\mu\text{m}$ wavelengths, respectively, putting the expected disk thickness slightly inside the PSF tail at the longest wavelengths.

For the closer galaxies, NGC 5236, NGC 4449 and NGC 5068, we should be able to resolve and distinguish a kink in the PS if it occurs at the disk thickness, which may range from ~ 200 pc for the spiral galaxy NGC 5236 to much larger values such as ~ 400 pc for the dwarfs. This dwarf thickness corresponds to an intrinsic ratio of axis of $q_0 = 0.44 \pm 0.20$ (Johnson et al. 2017) for a kpc-scale disk. Note that the separations between the blue lines in the images of these three galaxies are all about 1 kpc (see figure captions). Nevertheless, we do not see any obvious and systematic kinks in the 50-PS averages. The reason for this lack of an obvious kink could be that the PS varies too much from region to region. Extreme variations are partly the result of individual bright sources, which flatten the PS by dominating any fainter, possibly correlated structures from turbulence. Variations are also the result of the exponential disk profile, which steepens the PS because of its large scale in scans near the galaxy centers.

Figure 19 examines more closely whether there is a slope change in the range from 100 pc to 300 pc that might be indicative of disk thickness. The blue curve is the average of all the 50-PS slopes on scales larger than 200 pc, and the red curve is the average of all the 50-PS slopes smaller than 200 pc, down to 5 times the FWHM of the PSF (Table 1), which is about the limit of the PSF tail. These slopes are plotted versus wavelength for the four galaxies. The large-scale slope is comparable to (or slightly more negative than) the small-scale

slope at $5.6\mu\text{m}$, but at longer wavelengths, the PS slope is generally flatter on larger scales. For NGC 628, the slope difference is about constant with wavelength beyond $5.6\mu\text{m}$, suggesting that the increasing PSF width is not affecting the small-scale slope. The slope difference at these longer wavelengths is ~ 0.5 . The large-scale and small-scale slopes of the PS of scan 1550 in NGC 628, which contains the bright point-like source, are shown as circles in the upper left. As this scan best represents the effects of noise combined with the PSF, the slope difference is definitely not from disk thickness. Thus the other slope differences, which are about the same, are not likely to come from disk thickness either.

Aside from extreme variations in the PS with position, another explanation for the lack of an obvious kink is that most of the emission sources at the wavelengths considered here are closer to the midplane than expected. Previous PS with kinks tended to be based on diffuse gas that is traced by HI and cooler dust, and diffuse gas can be fairly thick. For example, the average hydrostatic equilibrium scale height for HI in 20 galaxies from The HI Nearby Galaxy Survey (THINGS) equals 330 pc (Bagetakos et al. 2011). In contrast, the star-forming regions seen in our passbands are probably connected with dense molecular clouds, which are typically close to the midplane.

The molecular cloud layer in the Milky Way has a FWHM thickness of ~ 100 pc in the main disk (Heyer & Dame 2015), which corresponds to a scale height, σ_z , of 42 pc for a Gaussian profile. This height is in agreement with simulations of a Milky Way type galaxy by Jeffreson et al. (2022), who got a molecular cloud scale height of 50 pc. In other measurements, Scoville et al. (1993) determined a FWHM of 220 pc ($\sigma_z = 84$ pc) in the edge-on galaxy NGC 891 using CO interferometry. This corresponds well with the half-width at half-maximum (HWHM) of 105 pc ($\sigma_z = 88$ pc) found by Elmegreen & Elmegreen (2020) for 133 star-forming cores in NGC 891 observed at $8\mu\text{m}$ with the Spitzer Space Telescope InfraRed Array Camera. Patra (2018) assumed hydrostatic equilibrium to derive the molecular HWHM in the highly inclined spiral galaxy NGC 7331, obtaining 50 pc - 80 pc at 6 kpc radius ($\sigma_z = 42$ pc - 67 pc). For NGC 6946, Patra (2021) measured a thin molecular HWHM of ~ 50 pc ($\sigma_z = 42$ pc) at 4 kpc radius, and found a second molecular disk that is thicker by a factor of 2 and coincides with the HI disk. Pety et al. (2013) previously found a similar two-component molecular disk in M51, with 2%-20% of the molecular gas at least 10 times thicker than the dense molecular gas. The molecular thicknesses in Ultra Luminous Infrared Galaxies seem to be larger than those in normal galaxies, perhaps because of additional forcing from galaxy interactions; Wilson et al. (2019) found an average hydrostatic equilibrium thickness for CO of ~ 180 pc in these galaxies.

Evidently, the molecular thicknesses in normal spiral galaxies correspond to inverse wavenumbers that can blend with the tail of the PSF, masking a slight change in PS slope. Molecular thicknesses in dwarfs are not as well known because CO emission is usually weak.

6.2. The Large-Scale Slope

The slope of the large-scale part of the PS contains information about the emission structure. These slopes

(on a log-log plot) range from approximately -0.6 at $21\mu\text{m}$ to -1.2 at $5.6\mu\text{m}$ (Table 2). The low- k/k_0 slope for dust emission in the LMC was -0.78 ± 0.19 at $24\mu\text{m}$, which is similar to ours in NGC 628 and NGC 5068 at $21\mu\text{m}$ in Table 2.

If we consider that the PS, $P(k)$, measures the combined product of the luminosity $L(k)$ of regions with size $D \sim 1/k$ multiplied by the number of these regions, $n(k)$, in the interval from k to $k + dk$, then

$$P(k) = L(k)n(k). \quad (3)$$

Writing $P(k) \propto k^{-\alpha-1}$ from our observations (i.e., the slope of the PS is $-\alpha$ on a log-log plot), $L(k) \propto k^\beta$, and $n(k) \propto k^\gamma$, we have $-\alpha - 1 = \beta + \gamma$. For a fully packed wavenumber space, $n(k) \propto k$ so $\gamma = 1$. Observations suggest a similar γ : the mass function for molecular clouds in a hierarchical ISM is $n(M)dM = M^{-x}dM$ where $x \sim 2$, and the mass-size relation from Larson's law, is $M \propto D^y$ with $y \sim 2$. These combine to give

$$\begin{aligned} n(D)dD &= n(M)dM \propto M^{-x}(dM/dD)dD \\ &\propto M^{-x}D^{y-1}dD = D^{-xy+y-1}dD \end{aligned} \quad (4)$$

and thus, after writing $n(k)dk = n(D)dD$ with $D = 1/k$,

$$\begin{aligned} n(k)dk &\propto D^{-xy+y-1}(dD/dk)dk \\ &\propto k^{xy-y+1}k^{-2}dk = k^{xy-y-1}dk \end{aligned} \quad (5)$$

so that $\gamma = xy - y - 1$. For $x = 2$ and $y = 2$ as suggested above for molecular clouds, $\gamma = 1$ again. The same values of x and y are observed for HII regions and their exciting star clusters in M51 (Scoville et al. 2001).

Now we see that the slope of the PS on a log-log plot, α , corresponds roughly to a size dependence of the region luminosity as $\beta = -\alpha - 1 - \gamma \sim -\alpha - 2$, in which case

$$L(D) \propto D^{-\beta} \propto D^{\alpha+1+\gamma} \sim D^{\alpha+2} \quad (6)$$

Since we measure $\alpha \sim 1$ from the average of all slopes in Table 2 at $5.6\mu\text{m}$ and $7.7\mu\text{m}$, $L(D) \propto D^3$ at the bluer wavelengths. We measure an average of $\alpha = 0.6$ at $21\mu\text{m}$ and then $L(D) \propto D^{2.6}$.

This size-luminosity relationship compares well with observations of HII regions in nearby galaxies. Liu et al. (2013) observed $L(D) \propto D^\eta$ for η between 2.5 and 3 using Pa α luminosities of HII regions in twelve galaxies. HII region luminosities may be a good tracer for the dust luminosities sampled by our PS because HII regions are marginally optically thick (Scoville et al. 2001; Hunt & Hirashita 2009). In our model, the shallower PS measured at longer wavelengths is the result of a shallower slope for $L(D)$, which means more extended IR radiation around star-forming regions at the longer wavelengths, probably corresponding to less local dust absorption of this radiation.

Equation 6 with its fractional power of D also suggests a fractal of dimension $\alpha + 2$. For the α measured by the slopes of our PS, this fractal dimension of 2.6 to 3 is comparable to the fractal dimension typically found for interstellar gas using other tracers and methods (e.g., Federrath et al. 2009; Elia et al. 2018).

7. CONCLUSIONS

Power spectra of three galaxies in the FEAST survey and one galaxy in the PHANGS survey, using infrared

wavelengths from $5.6\mu\text{m}$ to $21\mu\text{m}$ observed by JWST (Table 1), show no clear evidence for disk thickness in the form of an inflection point from the transition between two-dimensional turbulence on scales larger than the thickness and three-dimensional turbulence on scales smaller than the thickness. This lack of a clear inflection is partly the result of large variations in the PS from position to position, reflecting discrete bright sources which tend to flatten the large-scale PS and the exponential profiles of the galaxy disks, which tend to steepen the large-scale PS. In addition, the star-forming layers in these galaxies could be composed of dense gas that is several times thinner than the diffuse lower-density gas where PS kinks were previously found in different galaxies. This suggests that PS kinks for our galaxies could be blended with the extended tails of the JWST PSF.

The PS slopes on scales larger than 200 pc (Table 2) could be evidence for a source luminosity dependent on size, $L(D)$, which is proportional to size D to a power of around 3, in agreement with direct observations of this relationship elsewhere. Our shallower large-scale PS slope at longer wavelengths could then correspond to more extended NIR emission around star forming regions resulting from less local absorption.

Acknowledgements: This work is based in part on observations made with the NASA/ESA/CSA James Webb Space Telescope, which is operated by the Association

of Universities for Research in Astronomy, Inc., under NASA contract NAS 5-03127. These observations are associated with program #1783. Support for program #1783 was provided by NASA through a grant from the Space Telescope Science Institute, which is operated by the Association of Universities for Research in Astronomy, Inc., under NASA contract NAS 5-03127. Archival data presented in this paper were obtained from the Mikulski Archive for Space Telescopes (MAST) at the Space Telescope Science Institute. K.G. is supported by the Australian Research Council through the Discovery Early Career Researcher Award (DECRA) Fellowship (project number DE220100766) funded by the Australian Government and by the Australian Research Council Centre of Excellence for All Sky Astrophysics in 3 Dimensions (ASTRO 3D), through project number CE170100013. A.A. and A.P. acknowledge support from the Swedish National Space Agency (SNSA) through grant 2021-00108. A.A. acknowledges support by the Swedish research council Vetenskapsrådet (2021-05559). M.M. acknowledges financial support through grant PRIN-MIUR 2020SKSTHZ. ADC acknowledges the support from a Royal Society University Research Fellowship (URF/R1/191609).

Facility: JWST (NIRCam, MIRI). *Software:* JWST Calibration Pipeline (Bushouse et al. 2022; Grenfield & Miller 2016); SAOImage DS9 (Joye & Mandel 2003); FORTRAN, and VossPlot (Voss 1995).

REFERENCES

- Bacchini, C., Fraternali, F., Iorio, G., et al. 2020, *A&A*, 641, A70
 Bajaj, V. 2023, JWST Mosaic Sky Match, version 0.1, <https://github.com/Vb2341/jwst-mosaic-skymatch>
 Bagetakos, I., Brinks, E., Walter, F., et al. 2011, *AJ*, 141, 23. doi:10.1088/0004-6256/141/1/23
 Begum, A., Chengalur, J. N., & Bhardwaj, S. 2006, *MNRAS*, 372, L33
 Blagrove K., Martin P. G., Joncas G., Kothes R., Stil J. M., Miville Deschênes M. A., Lockman F. J., Taylor A. R., 2017, *ApJ*, 834, 126
 Block, D. L., Puerari, I., Elmegreen, B. G., & Bournaud, F. 2010, *ApJ*, 718, L1
 Bocchio, M., Bianchi, S., Hunt, L. K., & Schneider, R. 2016, *A&A*, 586, A8
 Bournaud, F., Elmegreen, B. G., Teyssier, R., Block, D. L., & Puerari, I. 2010, *MNRAS*, 409, 1088
 Burgers J.M., 1948. Elsevier, p. 171–199, 1, 0065-2156
 Bushouse, H., Eisenhamer, J., Dencheva, N., et al. 2022, JWST Calibration Pipeline, Zenodo, doi:10.5281/zenodo.7487203
 Calzetti, D., Adamo, A., Linden, S.T. 2024, arXiv2406.01831
 Chastenet, J., De Looze, I., Relaño, M., et al. 2024, arXiv:2408.08026
 Combes, F., Boquien, M., Kramer, C. et al. 2012, *A&A*, 539, A67
 Cook, D. O., Dale, D. A., Johnson, B. D., et al. 2014, *MNRAS*, 445, 899
 Dib, S., Braine, J., Gopinathan, M., et al. 2021, *A&A*, 655, A101. doi:10.1051/0004-6361/202141803
 Dutta, P., Begum, A., Bharadwaj, S., Chengalur, J. N. 2008, *MNRAS*, 384, L34
 Dutta, P., Begum, A., Bharadwaj, S., & Chengalur, J. N. 2009a, *MNRAS*, 397, L60
 Dutta, P., Begum, A., Bharadwaj, S., & Chengalur, J. N. 2009b, *MNRAS*, 398, 887
 Dutta, P., Begum, A., Bharadwaj, S., Chengalur, J.N. 2010, *MNRAS*, 405, L102
 Dutta, P., Begum, A., Bharadwaj, S., Chengalur, J.N. 2013a, *New Astronomy*, 19, 89
 Dutta P., Bharadwaj S., 2013b, *MNRAS*, 436, L49
 Dutta, P. 2015, *MNRAS*, 452, 803. doi:10.1093/mnras/stv1294
 Elia, D., Strafella, F., Dib, S., et al. 2018, *MNRAS*, 481, 509
 Elmegreen, B.G., Kim, S., & Staveley-Smith, L. 2001, *ApJ*, 548, 749
 Elmegreen, B. G., Elmegreen, D. M., & Leitner, S. N. 2003a, *ApJ*, 590, 271
 Elmegreen, B.G., Leitner, S.L., Elmegreen, D.M., & Cuillandre, J.-C. 2003b, *ApJ*, 593, 333
 Elmegreen, B. G. & Elmegreen, D. M. 2020, *ApJ*, 895, 71
 Federrath, C., Klessen, R. S., & Schmidt, W. 2009, *ApJ*, 692, 364
 Fensch, J., Bournaud, F., Brucy, N., et al. 2023, *A&A*, 672, A193
 Greenfield, P., & Miller, T. 2016, *A&C*, 16, 41
 Heyer, M., & Dame, T.M. 2015, *ARA&A*, 53, 583
 Hunt, L. K. & Hirashita, H. 2009, *A&A*, 507, 1327. doi:10.1051/0004-6361/200912020
 Jeffreson, S. M. R., Sun, J., & Wilson, C. D. 2022, *MNRAS*, 515, 1663. doi:10.1093/mnras/stac1874
 Johnson, M. C., Hunter, D. A., Kamphuis, P., et al. 2017, *MNRAS*, 465, L49
 Joye, W. A., & Mandel, E. 2003, in ASP Conf. Ser. 295, *Astronomical Data Analysis Software and Systems XII*, ed. H. E. Payne, R. I. Jedrzejewski, & R. N. Hook (San Francisco, CA: ASP), 489
 Koch, E.W., Chiang, I.-D., Utomo, D., Chastenet, J., Leroy, A.K., Rosolowsky, E.W., Sandstrom, K.M. 2020, *MNRAS*, 492, 2663
 Kolmogorov AN. 1941, reprinted in 1991 *Proc. Roy. Soc. London A*. 434:9-13
 Lazarian A., Pogosyan D., 2000, *ApJ*, 537, 720
 Lee, J.C., Sandstrom, K.M., Leroy, A.K. et al. 2023, *ApJ*, 944, 17L
 Leroy, A. K., Schinnerer, E., Hughes, A., et al. 2021, *ApJS*, 257, 43
 Liu, G., Calzetti, D., Kennicutt, R. C., et al. 2013, *ApJ*, 772, 27
 Muller, E., Stanimirović, S., Rosolowsky, E., Staveley-Smith, L., 2004, *ApJ*, 616, 845
 Nandakumar, M., Dutta, P. 2020, *MNRAS*, 496, 1803
 Nandakumar, M. & Dutta, P. 2023, *MNRAS*, 526, 4690
 Nestingen-Palm, D., Stanimirović, S., González-Casanova, D. F., et al. 2017, *ApJ*, 845, 53
 Padoan, P., Kim, S., Goodman, A., Staveley-Smith, L. 2001, *ApJ*, 555, L33

Patra, N. N. 2018, MNRAS, 478, 4931.
doi:10.1093/mnras/sty1512

Patra, N. N. 2021, MNRAS, 501, 3527

Pety, J., Schinnerer, E., Leroy, A. K., et al. 2013, ApJ, 779, 43.
doi:10.1088/0004-637X/779/1/43

Pingel, N.M., Dempsey, J., McClure-Griffiths, N.M. et al. 2022, PAS Australia, 39, e005

Scoville, N. Z., Thakkar, D., Carlstrom, J. E., & Sargent, A. I. 1993, ApJ, 404, L59

Scoville, N. Z., Polletta, M., Ewald, S., et al. 2001, AJ, 122, 3017

Stanimirović S., Staveley-Smith L., Dickey J. M., Sault R. J., Snowden S.L., 1999, MNRAS, 302, 417

Stanimirović, S. & Lazarian, A. 2001, ApJ, 551

Stanimirović, S., Staveley-Smith, L., van der Hulst, J. M., Bontekoe, T.J. R., Kester, D. J. M., Jones, P. A. 2000, MNRAS, 315, 791

8. APPENDIX

Szotkowski, S., Yoder, D., Stanimirović, S., et al. 2019, ApJ, 887, 111

Tully, R. B., Rizzi, L., Shaya, E. J., et al. 2009, AJ, 138, 323

Tully, R. B., Courtois, H. M., Dolphin, A. E., et al. 2013, AJ, 146, 86.

van den Bergh, S. 1988, PASP, 100, 344

Verbeke, R., Papastergis, E., Ponomareva, A. A., et al. 2017, A&A, 607, A13

Voss, R. 1995, VossPlot: A Software Tool for Scientific and Technical Graphics, Springer, ISBN-13 978-0387142159

Willett, K. W., Elmegreen, B. G., & Hunter, D. A. 2005, AJ, 129, 2186

Williams, T. G., Lee, J. C., Larson, K. L., et al. 2024, ApJS, 273, 13

Wilson, C. D., Elmegreen, B. G., Bemis, A., et al. 2019, ApJ, 882

Zhang H.-X., Hunter D. A., Elmegreen B. G., 2012, ApJ, 754, 29

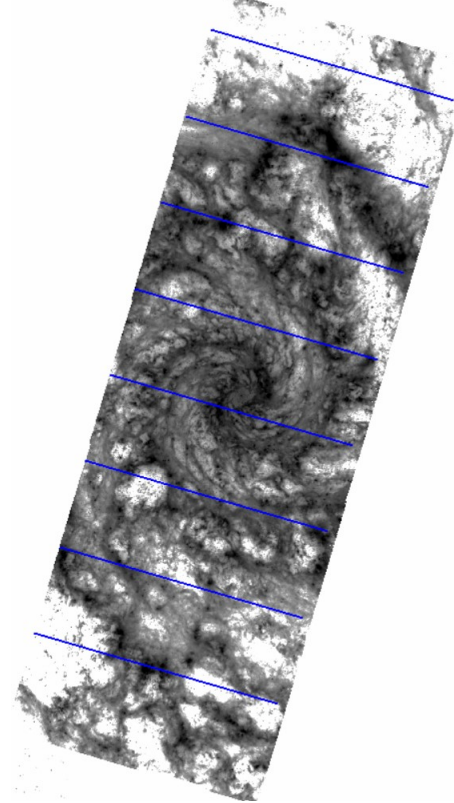


FIG. 1.— Appendix Figure 1: NGC 628 at $7.7\mu\text{m}$ with sample scan directions like those used to determine the PS, as in Fig. 2.

This paper was built using the Open Journal of Astrophysics \LaTeX template. The OJA is a journal which provides fast and easy peer review for new papers in the `astro-ph` section of the arXiv, making the reviewing process simpler for authors and referees alike. Learn more at <http://astro.theoj.org>.

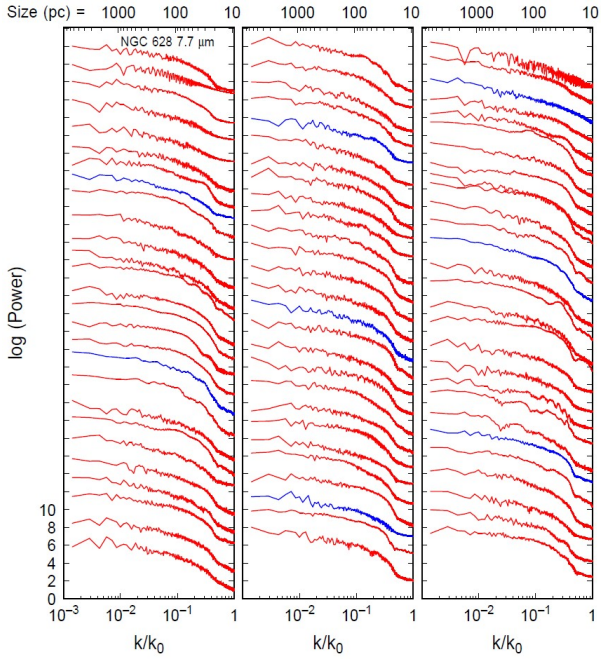


FIG. 2.— Appendix Figure 2: The same as Fig. 6 but at $7.7\mu\text{m}$.

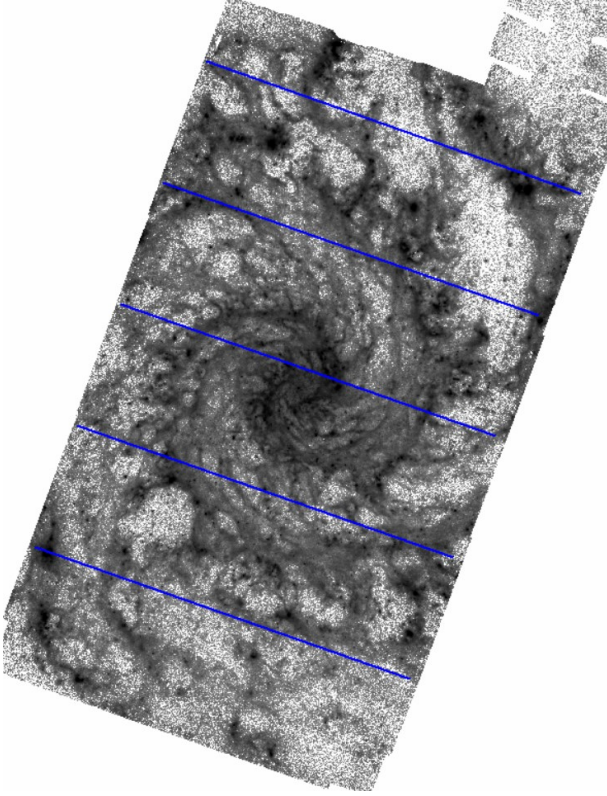


FIG. 3.— Appendix Figure 3: NGC 628 at $10\mu\text{m}$ with sample scan directions like those used to determine the PS, as in Fig. 2. The lines are separated by 500 pixels, which is $40''$ and 1.91 kpc.

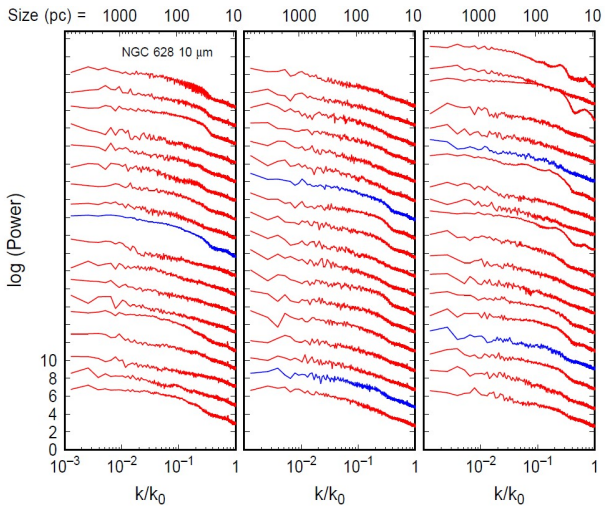


FIG. 4.— Appendix Figure 4: The same as Fig. 6 but at $10\ \mu\text{m}$.

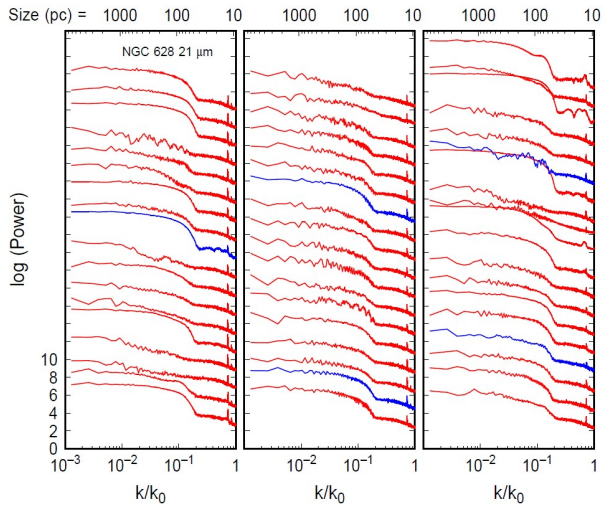


FIG. 5.— Appendix Figure 5: The same as Fig. 6 but at $21\ \mu\text{m}$.

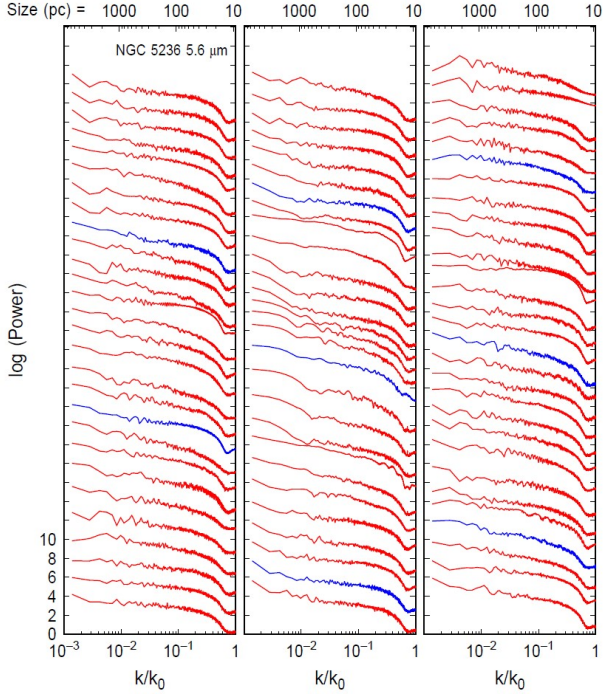


FIG. 6.— Appendix Figure 6: Averages of each 50 adjacent PS covering the NGC 5236 image in Fig. 12, shifted vertically for clarity. The 50-PS average corresponding to the southwest part of the image is at the bottom of the left-hand panel. Higher in the same panel, and then from bottom to top in the middle panel and bottom to top in the right-hand panel are the 50-PS averages in sequence from southwest to northeast in the image.

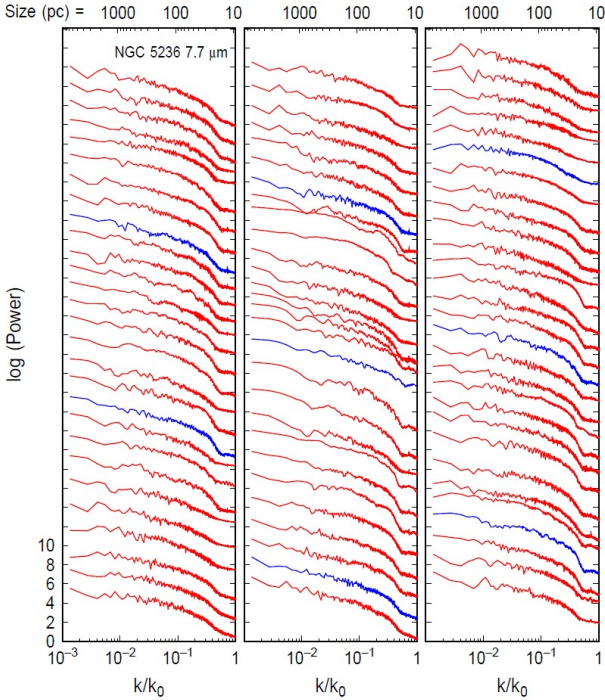


FIG. 7.— Appendix Figure 7: Same as Fig. 6 for NGC 5236 but at $7.7\mu\text{m}$.

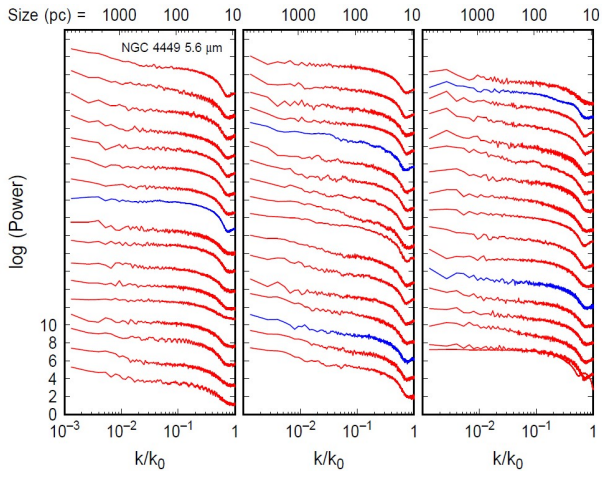


FIG. 8.— Appendix Figure 8: Averages of each 50 adjacent PS for the minor axis scans covering the $5.6\mu\text{m}$ image in the left-hand panel of Fig. 14. Scans go from southwest in the lower part of the left-hand panel to northeast in the upper part of the right-hand panel.

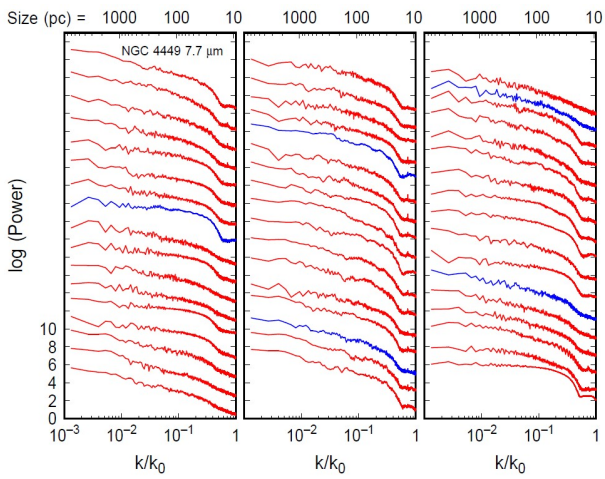


FIG. 9.— Appendix Figure 9: Same as Fig. 8 but for $7.7\mu\text{m}$.

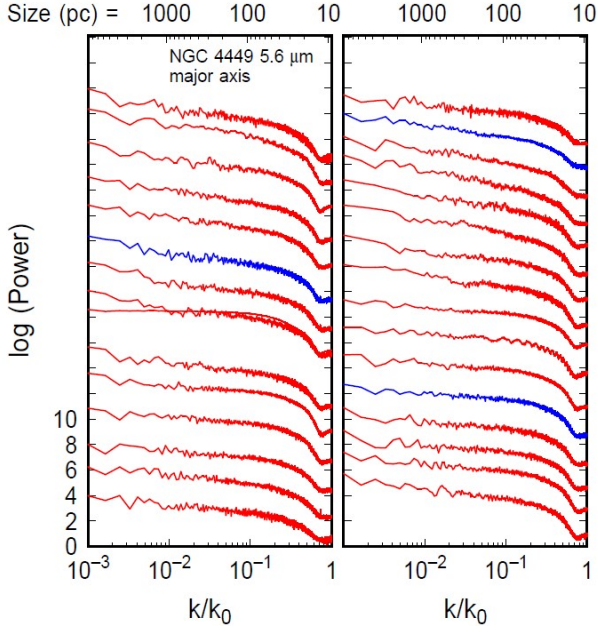


FIG. 10.— Appendix Figure 10: Averages of each 50 adjacent PS for the major axis scans covering the $5.6\mu\text{m}$ image in Fig. 14.

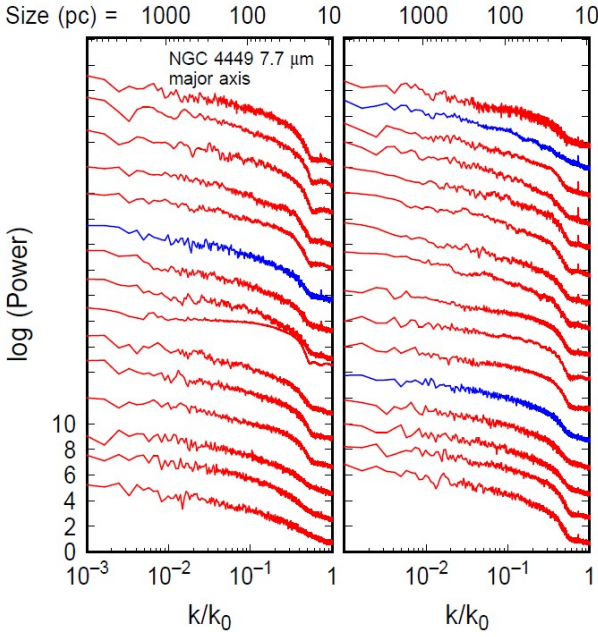


FIG. 11.— Appendix Figure 11: Averages of each 50 adjacent PS for the major axis scans covering the $7.7\mu\text{m}$ image in Fig. 14.

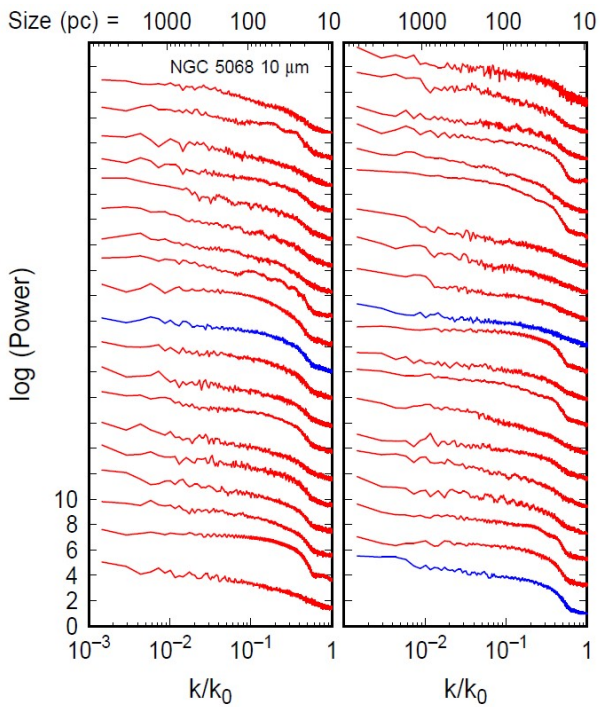


FIG. 12.— Appendix Figure 12: Averages of each 50 adjacent PS for the $10\mu\text{m}$ image of NGC 5068 in Fig. 17. Scans go from southeast in the lower part of the left-hand panel to northwest in the upper part of the right-hand panel.

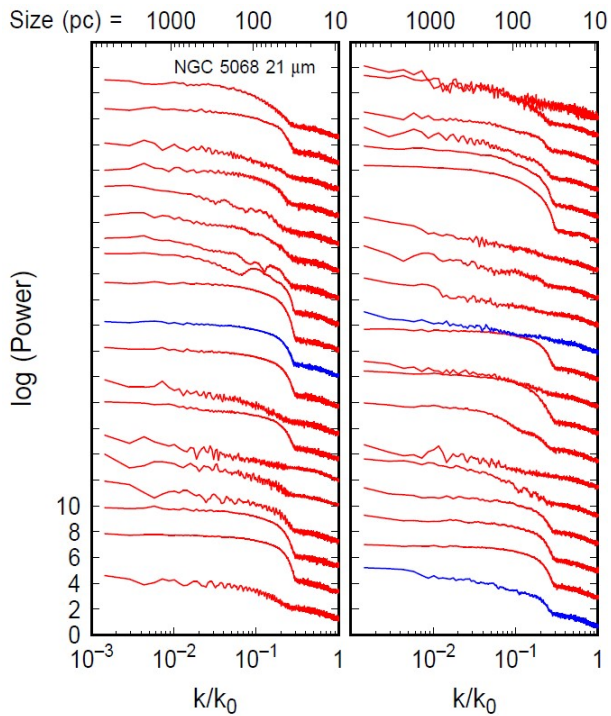


FIG. 13.— Appendix Figure 13: Averages of each 50 adjacent PS for the $21\mu\text{m}$ image of NGC 5068.